



HAL
open science

Magnetization transfer from inhomogeneously broadened lines (ihMT): Improved imaging strategy for spinal cord applications

Olivier M. Girard, Virginie Callot, Valentin H. Prevost, Benjamin Robert, Manuel Taso, Guilherme Ribeiro, Gopal Varma, Novena Rangwala, David C. Alsop, Guillaume Duhamel

► To cite this version:

Olivier M. Girard, Virginie Callot, Valentin H. Prevost, Benjamin Robert, Manuel Taso, et al.. Magnetization transfer from inhomogeneously broadened lines (ihMT): Improved imaging strategy for spinal cord applications. *Magnetic Resonance in Medicine*, 2016, pp.n/a–n/a. 10.1002/mrm.26134 . hal-01425518

HAL Id: hal-01425518

<https://amu.hal.science/hal-01425518>

Submitted on 24 Jan 2022

HAL is a multi-disciplinary open access archive for the deposit and dissemination of scientific research documents, whether they are published or not. The documents may come from teaching and research institutions in France or abroad, or from public or private research centers.

L'archive ouverte pluridisciplinaire **HAL**, est destinée au dépôt et à la diffusion de documents scientifiques de niveau recherche, publiés ou non, émanant des établissements d'enseignement et de recherche français ou étrangers, des laboratoires publics ou privés.

Magnetization Transfer from Inhomogeneously Broadened Lines (ihMT): Improved Imaging Strategy for Spinal Cord Applications

O.M. Girard^{1,2}, V. Callot^{1,2}, V.H. Prevost^{1,2}, B. Robert³, M. Taso^{1,2,4}, G. Ribeiro^{1,2}, G. Varma⁵, N. Rangwala⁵, D.C. Alsop⁵ and G. Duhamel^{1,2}

¹ Aix-Marseille Université, CRMBM, UMR 7339 CNRS – AMU, Marseille, France

² Pôle d'Imagerie Médicale, CEMEREM, AP-HM, Marseille, France

³ Siemens Healthcare, Saint-Denis, France

⁴ Aix-Marseille Université, IFSTTAR, LBA UMR T24, Marseille, France

⁵ Department of Radiology, Beth Israel Deaconess Medical Center, and Harvard Medical School, Boston, MA USA

Corresponding author:

Olivier M. Girard, PhD
Aix-Marseille Université
Centre de Résonance Magnétique Biologique et Médicale
CRMBM - CEMEREM, UMR 7339 CNRS - Faculté de Médecine
27 Boulevard Jean Moulin, 13385 Marseille Cedex 5, France
E-mail: olivier.girard@univ-amu.fr

Paper type: Full paper

Word count of manuscript body:

Word Count: 5191

Number of figures: 7

Number of tables: 0

Abstract:

Purpose: Inhomogeneous magnetization transfer (ihMT) shows great promise for specific imaging of myelinated tissues. Whereas the ihMT technique has been previously applied in brain applications, the current report presents a strategy for cervical spinal cord (SC) imaging free of cerebrospinal fluid (CSF) pulsatility artifacts.

Methods: A pulsed ihMT preparation was combined with a single-shot HASTE readout. ECG synchronization was used to acquire all images during the quiescent phase of SC motion. However ihMT signal quantification errors may occur when a variable recovery delay is introduced in the sequence as a consequence of variable cardiac cycle. A semi-automatic retrospective correction algorithm, based on TR-matching, is proposed to correct for signal variations of long T_1 -components (e.g. CSF).

Results: The proposed strategy combining ECG synchronization and retrospective data pairing led to clean SC images free of CSF artifact. Lower variability of the ihMT metrics were obtained with the correction algorithm, and allowed for shorter TR to be used, hence improving SNR efficiency.

Conclusion: The proposed methodology enabled faster acquisitions, while offering robust ihMT quantification and exquisite SC image quality. This opens great perspectives for widening the *in vivo* characterization of SC physiopathology using MRI, such as studying WM tracts microstructure or impairment in degenerative pathologies.

Key words:

Spinal cord, inhomogeneous magnetization transfer, CSF pulsatility, ECG synchronization, motion correction, myelin, white matter

Introduction

Inhomogeneous magnetization transfer (ihMT) shows great promise for central nervous system (CNS) imaging thanks to its apparent high myelin specificity compared to conventional magnetization transfer (MT) (1,2). Although important milestones, such as the development of a theoretical model (3), have been achieved, thorough understanding of the ihMT effect is still in an early phase. The high specificity of ihMT toward myelin is presumably attributed to its unique architecture, consisting of multiple sheaths of lipid bilayers, and specific molecular composition, notably high lipid and relatively low protein content (4,5). Whereas proton-proton dipolar interaction usually results in homogeneous broadening (6) of the NMR spectrum for large macromolecules, the rapid axial rotation of the lipid chains composing the myelin results in inhomogeneous broadening for biological membranes (7,8). In addition multiple mechanisms such as spin diffusion, chemical exchange and molecular motion, which usually tend to homogenize broad semi-solid NMR lines in tissue, seem highly constrained or inefficient in the case of myelin sheath environment. Molecular motions within lipid bilayers are restricted as compared to free lipids, water exchange from the myelin water to the bulk water is relatively slow (9), and spin diffusion within lipid membranes is a slow process (10). Altogether, these evidences strongly support the myelin spectrum being inhomogeneous on the time scale of several milliseconds, in compliance with the recent measure and sensitivity demonstration of the ihMT effect *in vivo*.

So far the ihMT technique has been successfully applied for brain applications at various field strengths, including clinical 1.5T (2) and 3T (1) as well as preclinical 11.75T (11). Initial reports concerned both methodological developments and applications to demyelinating pathologies such as multiple sclerosis (12,13). In addition, recent preliminary studies have also described the feasibility of ihMT for spinal cord (SC) investigations (14,15), which is of the utmost importance since the technique may open new perspectives to better describe the SC healthy structure and its pathological alterations. Challenges for SC ihMT studies include a relatively coarse resolution compared to the small size of the cord, the presence of susceptibility effects from surrounding tissues (e.g. bones), and most importantly sensitivity to the pulsatility of the cerebrospinal fluid (CSF), which induces motion in and around the cord (16). Indeed, in comparison with conventional MT, such motion may have more dramatic impact on ihMT because it has lower sensitivity (ihMT signal on the order of 10% of the unsaturated signal) and requires data subtraction from multiple images potentially acquired at different phases of

motion. Hence, as has been observed in DTI studies (17,18), pulsatile motion could have critical effects on SC image quality and potential contamination of SC tissue signal may lead to inaccurate ihMT quantification.

The current report expands on earlier work (15) and presents a complete strategy for cervical SC ihMT imaging free of CSF pulsatility artifacts. The proposed method combines electro-cardiogram (ECG) synchronization and retrospective data pairing. This strategy aims at correcting for signal variations of long T_1 -components, such as CSF, that occur when a variable recovery delay is introduced in the sequence as a consequence of variable cardiac cycle. In comparison with other strategies correcting for such T_1 -recovery effects (19,20), the proposed method is model-free as it simply matches images acquired with a similar recovery period. A semi-automatic algorithm for data correction is presented along with accurate ihMT ratio quantification of the cord.

Methods

All experiments were performed at 1.5T (Siemens Avanto, Erlangen, Germany) on healthy volunteers, in compliance with guidelines from our institutional committee on clinical investigations.

ihMT magnetization preparation

A pulsed ihMT preparation module was used, as described previously (2). The ihMT contrast generation relies on the comparison of two different MT weighted images (1): one using a single-frequency offset ($+\Delta f$) leading to the saturated image MT^+ and the other using a dual-frequency offset and identical total energy ($+\Delta f$ and $-\Delta f$ applied sequentially) leading to the saturated image MT^{+-} . In order to compensate for potential MT asymmetry effects (1,15), two additional single (MT^-) and dual-frequency (MT^{-+}) acquisitions are measured and the final ihMT image is generated by the following combination:

$$ihMT = MT^+ + MT^- - MT^{+-} - MT^{-+} \quad \text{Eq. 1}$$

Note that both dual-frequency saturation weighted images, MT^{+-} and MT^{-+} , are essentially similar. The ihMT ratio is defined by $ihMTR = ihMT/S_0$, where S_0 is the signal measured with RF saturation power set to zero.

The following parameters were used, derived from brain imaging optimization at 1.5T (2): frequency offsets $\pm\Delta f = \pm 7\text{kHz}$, pulsewidth $p_w = 500\mu\text{s}$ and interpulse repetition time $\Delta t = 1\text{ms}$. The total saturation time (τ), optimized at $\tau = 700\text{ms}$ for brain studies, had to be adapted to the ECG synchronization required in SC imaging in order to ensure acquisition of the image during the quiescent phase of the cervical spinal cord. This phase starts on average about 300ms after the R-wave and lasts around 50% of the whole cardiac cycle (17) (typically in the range of 800-1100ms). Hence the MT saturation, triggered by the R-wave, was reduced to $\tau = 500\text{ms}$, i.e. leaving about 200-350ms for image readout during the quiescent phase. The time-integrated squared B_1 (i.e. the average RF energy absorbed during the saturation period τ , noted E_{TR}) was adjusted so that the RF energy of the saturation pulsed train corresponded to $E_{TR} = 17.2\mu\text{T}^2\cdot\text{s}$. This value is lower than the optimized value used for brain ($E_{TR} \geq 30\mu\text{T}^2\cdot\text{s}$), hence slightly reducing the sensitivity of the technique (see Fig. 7 of reference (2)). However this reduced E_{TR} value was chosen to allow scanning under regulatory Specific Absorption Rate (SAR) limitations for all the investigated nominal repetition times (TR) down to 2500ms.

Imaging

A product 12-channel head / 4-channel neck combined coil was used for the entire study. The ihMT preparation was combined with a single-shot 2D HASTE readout module, to provide low sensitivity to susceptibility effects, high SNR and rapid acquisition time, desirable features for SC imaging optimization. Such readout, however, is only suitable for single-slice imaging because of rather long echo-train duration. The sagittal plane was chosen to acquire simultaneously signals from cervical spinal cord levels C2-C4 and from a reference brain area (i.e. the corpus callosum – CC). The following parameters were used: 25cm Field-Of-View, 192×192 matrix size, 1.3mm in-plane resolution, 789Hz/pixel bandwidth, 120° refocusing flip angles, no parallel acceleration. Partial volume effects due to WM/GM structure distribution within the SC were assessed using two different slice thicknesses: 5mm and 8 mm. In addition, potential blurring effects related to the long HASTE readout echo-train were assessed by applying Phase-Encoding (PE) in the Antero-Posterior (A-P) and the Superior-Inferior (S-I) directions. For the S-I direction, 50% phase oversampling was prescribed to prevent aliasing. The shortest possible echo times (TEs) were used, corresponding to 31ms in the S-I direction (for a total echo-train length of $\sim 550\text{ms}$), and to 20ms in the A-P direction (echo-train length of $\sim 365\text{ms}$). 50% phase oversampling was also tested in the A-P direction to provide a fair comparison (similar TE settings as in the S-I direction).

Image acquisition was synchronized to the ECG and four nominal TR settings were studied: TR=2500, 3500, 4500 and 10000 ms. The latter configuration corresponded to a reference acquisition, for which full recovery of the longitudinal magnetization is expected for all human tissues including CSF. For each scan, ECG physiological data and trigger instances were recorded in a log file throughout the scan in order to allow further retrospective data correction.

In order to increase the signal-to-noise ratio (SNR) of the ihMT images, 30 signal averages (NEX) of each of the four kinds of MT weighted images (see Eq. 1) were acquired for all conditions (except for the reference acquisition – i.e. TR=10000ms, for which 20 NEX were acquired to reduce scan time), and 3 NEX for S_0 . Overall, the total number of images per studied condition was 123 images (83 for TR=10000ms), leading to ~ 6.5 min, 8.5 min, 10.5 min and 14.5 min total acquisition time for TR of 2500, 3500, 4500 and 10000 ms, respectively. Each aforementioned imaging condition was tested on three healthy volunteers (males, 33 ± 6 y.o.).

Post-Processing

Because of the small size of the SC, only ~ 4-6 pixels covered its antero-posterior extension for the 1.3mm in-plane resolution used in this study, and hence, significant Gibbs' ringing occurred. This well-known MR artifact can have dramatic impact on SC image quality because it adds a non-local signal component corresponding to signal secondary-lobes coming from neighboring tissues. These lobes typically arise 1-2 voxel away from edges, and hence tend to add CSF signal onto the SC which should be avoided in the current study which aims to measure unbiased SC ihMT metrics.

Windowing the k-space data helps to strongly attenuate these confounding signal oscillations and also improves SNR at the same time, although at the cost of a broadening or blurring of the main lobe, causing a loss in spatial resolution. Here a Hamming-shape window was used, offering a fair compromise between secondary lobe attenuation and blurring (21). The full width at half maximum corresponds to $1.81 \times$ the nominal resolution as compared to 1.21 for unfiltered data, resulting in a reduction of the effective resolution by a factor of 1.5. Additionally, a zero-filling factor of 2 was used for selection of regions-of-interest (ROIs) and subsequent quantitative measurements. The effect of k-space windowing is illustrated in Fig. 1.

The multiple averages of the different instances of the S_0 and MT weighted images were all registered together using the SPM8 realign routine (22) prior to image combination.

ECG synchronization and retrospective data pairing

Image acquisition synchronized with ECG led to effective TR values that depend on the cardiac cycle. Here, the trigger initiated the ihMT preparation module and the variable delay was placed after the readout, hence lengthening the signal recovery period. Any TR variation from one image acquisition to the other directly translates into different T_1 -weighting of long T_1 components (e.g. CSF) in individual MT images (except for the fully-relaxed acquisition). The result of combining all the MT images regardless of their actual TR values would induce errors in the ihMT signal because it relies on image subtraction (see Eq. 1). In particular, the CSF compartment may give rise to an artefactual non-zero ihMT signal, which could affect SC tissue conspicuity and ihMT metrics because of partial volume effects.

A custom retrospective pairing algorithm was developed in MATLAB (R2010b, The MathWorks Inc., Natick, MA, USA) and tested to correct for such residual errors in the ECG-triggered ihMT images. The proposed algorithm basically works by extracting the actual TR values from the recorded physiological data, and then applying a lookup loop to generate pairwise TR-matched MT images when processing the ihMT subtraction image from Eq. 1 (i.e. a dual frequency MT image subtracted from a single frequency image with identical TR).

In order to select data from the whole ihMT dataset, all instances of each of the four MT weighted images used in Eq. 1 were considered along with their corresponding actual TR value: $[TR_1, MT_1^+]$ would be considered for the first MT weighted image acquisition, $[TR_i, MT_i^{+-}]$ would be considered for i^{th} acquisition. Then the algorithm considered a single saturation MT image, e.g. $[TR_1, MT_1^+]$, and searched for a matched TR within all instances of MT^{+-} and MT^{++} . When a match was found, e.g. for the j^{th} image index, $[TR_j, MT_j^{+-}]$, the two images were coupled together and stored aside. The same process was repeated among the remaining single- and dual-saturation MT dataset until a maximum number of image pairs were generated. After the whole process, images that could not be paired were discarded from the final dataset and were not considered to form the composite ihMT image, hence leading to SNR loss. Thus, in order to prevent a too restrictive matching process, a tolerance margin δTR was used so that the TR matching condition was defined as $TR \pm \delta TR$.

Semi-automation for optimal subject- and scan- dependent pairing

A total number of 67 δTR values were tested according to the following scheme: δTR varied in 2.5ms-step from 0 to 25ms, then in 5ms-step up to 50ms, in 10ms-step up to 100ms, in 25ms-step up to 500ms and in 50ms-step up to 2000ms. Note that 2.5ms corresponded to the temporal resolution of the physiological data recording, whereas $\delta TR=2000ms$ was appropriate

to cover the entire range of actual TRs (i.e. not to exclude any data through the pairing algorithm) for the majority of experimental scenarios, including the trigger missing an R-wave because of poor ECG signal quality. For each δTR value, the retrospective pairing algorithm was applied and the corresponding ihMT and ihMTR maps were generated and stored along with the number of paired images from the whole dataset, defined as $\text{NEX}_{\delta\text{TR}}$.

From these multiple available ihMT datasets the selection criterion was designed as a trade-off between negligible residual ihMT signal in CSF (defined as ϵ , such that $|\text{ihMTR}_{\text{CSF}}| < \epsilon$) and highest SNR in SC. For that purpose, ROIs were manually selected on the average S_0 image in the CSF and SC (covering levels C2 to C4) areas and used to measure the ihMT metrics (i.e. both ihMTR and SNR) across the entire dataset (identical ROIs were used for all δTR values). ROIs were drawn slightly away from the structure edges to prevent partial volume effects due to blurring from neighboring tissues. Although refined modeling accounting for the coil configuration and acquisition strategy would be necessary for accurate SNR calculation, a simple estimation was used in the current study, defined as the mean ihMT signal in the ROI divided by the noise standard deviation measured in a large signal-free area on the same image, located in the neck posterior side. In practice, three values of ϵ were systematically evaluated: 0.1, 0.3 and 0.5%. For each ϵ , the algorithm looped over all δTR values and tested for the $|\text{ihMTR}_{\text{CSF}}| < \epsilon$ condition; and finally among the datasets satisfying the latter condition, the algorithm selected the dataset providing the highest SNR in the SC ROI.

IhMTR measurements were also performed in the genu of the corpus callosum (CC), considered as a control structure because it provides high ihMT signal while being less prone to CSF motion and partial volume than SC.

Results

Typical images obtained with and without ECG synchronization are shown on Fig. 2. Whereas unsynchronized MTR data (2d and 2e) do not show obvious signs of motion as compared to ECG-triggered acquisitions (2b), the effect of the CSF pulsatility is particularly strong on ihMT images (2f and 2g), where artifacts are clearly noticeable in the cervical area (green arrows). Conversely, the strategy combining ECG-synchronization and retrospective filtering leads to clean SC ihMT signal free of CSF artifacts (2c).

Typical measurements of MT^+ , MT^- , MT^{+-} and MT^{-+} across the different repetitions are shown in Fig. 3 for CSF, SC and CC. Using no ECG-synchronization, little signal difference

between MT weighted signals was present in CSF (3a), consistent with expected zero-ihMT effect in this structure. SC MT signals (3b) demonstrated poor separation of the single-frequency data from the dual-frequency data, consistent with CSF pulsatility effects. Conversely, in CC, a clean separation of these data was observed (3c), emphasizing little CSF motion near this structure. Image acquisition synchronized with ECG led to variable TR and hence to different T_1 -weightings, which translated into additional signal recovery for increasing TR in CSF (3d). Noteworthy little signal difference was observed between the MT signal data clouds, again consistent with no ihMT effect expected in CSF. For SC, the signal separation between single frequency and dual frequency MT images was clearly evident (3e). Of interest, the mild signal recovery with increasing TR in SC suggested partial volume effects with long T_1 components, presumably from CSF. Lower signal variations with TR were obtained in CC (3f), consistent with reduced partial volume effects. Besides, the intensity of the ihMT effect, which corresponds to the signal difference between single- and dual-frequency saturation, appeared similar for CC for both triggered and non-triggered acquisitions, again consistent with low pulsatile motion in this area.

Requirement for the TR-matching process may be instinctively appreciated from Fig. 3, and the automation procedure is illustrated in Fig. 4 where two particularly striking cases are displayed. Whereas no ihMT signal is expected in the CSF compartment, ECG rate fluctuations may induce a strong residual ihMT signal in CSF when no TR-matching is used. The quasi-random nature of these fluctuations makes the artifactual CSF signal either positive (as in (4d)) or negative (as in (4f)), in relation to the average TR of the single- and dual-saturation MT image datasets. The impact of the δTR value on the resulting ihMTR in CSF and SC, on the number of preserved NEX and on the ihMT SNR in SC is demonstrated on the curves. In Fig. (4a) (positive CSF bias), starting from the right side, ($\delta TR=1000ms$, no data exclusion: $NEX_{\delta TR} = \text{total number of NEX} = 120$), the algorithm progressively discards non TR-matched data-pairs as δTR is shortened, making the CSF ihMTR decrease and tend towards zero. The SC ihMTR progressively decreases as well towards a stable value as δTR is shortened, showing a similar trend as CSF and suggesting partial volume effect. For very short δTR (e.g. $<50ms$ here) the SC ihMT SNR drops because of high number of excluded pairs. Using a threshold value of $\epsilon = 0.3\%$ for the CSF signal, the algorithm converges toward the optimal dataset corresponding to $\delta TR=50ms$ and $NEX_{\delta TR} = 110$. The corresponding ihMTR map demonstrated improved conspicuity of the SC and brain tissue (4c). Similar behavior of the TR-filtering algorithm occurs for the negative CSF bias case (4b). The CSF ihMT signal progressively increases towards zero as δTR decreases, and the SC ihMTR converge to a baseline value, again

consistent with CSF partial volume. For very short δTR (e.g. < 20 ms here) the actual value of $ihMTR_{CSF}$ was not stable, consistent with poor SNR due to excessive data exclusion during the pairing process. Using $\varepsilon = 0.3\%$, the optimal dataset corresponded to $\delta TR=35ms$ and $NEX_{\delta TR}=92$. Similar to the positive case, the $ihMTR$ map resulting from this correction greatly improved the SC delineation (4e) compared to that of the unpaired data, where the strong negative signal from CSF contaminates the cord signal. Finally, one can appreciate the similarities between the two TR-matched datasets in (4c) and (4e) as well as the strong differences between the unpaired ones in (4d) and (4f).

Comparison between acquisitions performed using different nominal TR values further demonstrated the efficiency of the proposed TR-filtering strategy for various T_1 -weighting conditions (Fig. 5). Regardless of the intensity of CSF T_1 -recovery effects (strong in (5a), moderate in (5b), and very low in (5c)), the best TR-matched images ((5g)-(5i)) demonstrated a similar quality to that of the non TR-matched full relaxation image (5f), here taken as a reference due to almost constant CSF signal for $TR > 10000ms$. Conversely, without TR-matching and for short nominal TR, the CSF residual signal greatly decreased the image quality ((5d) and (5e)).

Fig. 6 and 7 summarizes the main quantitative findings observed on the 3 healthy volunteers for all the investigated sets of parameters. Results are indicated as mean value \pm standard error of the mean, calculated for the selected ROIs over the three volunteers. Panels (6a) and (6b) focus on $ihMTR$ metrics obtained without and with the TR-matching strategy. For all TR cases the $ihMTR$ values measured in SC with 8mm slice thickness were slightly lower (red curves) than that with 5mm slice thickness (blue curves). When no TR-matching was used (6a), the CSF $ihMT$ signal measured for nominal TRs $< 4s$ was not stable, demonstrating strong signal fluctuations (very large error bars, up to 2.7% absolute scale), and causing increased variability of the SC data as well (relatively large error bars, up to 1% absolute scale). Note that the error bars correspond to the dispersion of the $ihMTR$ values across volunteers, hence emphasizing poor robustness. Conversely, with the TR-matching strategy (6b) and the CSF $ihMT$ signal constrained to $0\pm\varepsilon\%$, variations of the $ihMTR$ signals greatly decreased in the SC (maximum error bar of 0.5%), thus improving $ihMTR$ measurement stability across all nominal TRs.

The SNR efficiency, defined as the SNR of $ihMT$ measurement obtained per total scan time (i.e. $SNR/\sqrt{T_{acq}}$), is presented in (6c). Despite data-pair exclusions, the TR-matching strategy combined with the use of shorter TR values generally allowed greatly improved SNR

efficiency (roughly doubled from TR = 10000ms to TR = 3500ms for 5mm slice thickness, blue curve). Of interest, data showed low inter-subject variations down to a TR of 3500ms, whereas stronger variability occurred for 2500ms nominal TR.

Finally, Fig. (7a) compares ihMT ratios measured for the different phase encoding conditions (A-P, A-P +50% phase oversampling and S-I) for both SC and the reference CC structure. Whereas CC measurements were similar for the three PE conditions, SC measurements in the S-I direction (ihMTR $\approx 7.8 \pm 0.3\%$) demonstrated a clear increase as compared to those in the A-P direction both without (ihMTR $\approx 6.3 \pm 0.4\%$, $p < 0.05$) and with 50% PE oversampling (ihMTR $\approx 5.8 \pm 0.4\%$, $p < 0.01$).

Discussion

Whereas non ECG-triggered SC acquisitions may be exploitable on some rare occasions (e.g. when the subject heart rate is particularly stable and synchronous with TR over the whole scan time), a prohibitively strong variability of SC signal was often observed over multiple NEX acquisitions, hence driving the need for an alternative SC ihMT imaging strategy. Such a strong sensitivity to motion is a consequence of the image combination (i.e. subtraction) required to generate the composite ihMT images. Overall, the hereby proposed correction method demonstrated good efficiency with ECG-synchronization able to remove CSF-pulsatility artifacts (Figs. 2 and 3) and TR-matching process able to remove undesirable residual CSF signal occurring for incomplete CSF signal recovery (Figs. 4-6). Although the latter feature moderately affected the quantification of ihMTR values within cervical SC on average (Figs. (6a) vs. (6b)), the conspicuity of the SC was strongly affected on some occasions (Fig. 4) and the metric variability increased when no TR-matching was used (large error bars in (6a)), consistent with partial volume with CSF. Besides, an optimal protocol should provide high fidelity signal for both SC and CSF and good robustness, especially in the clinical context where accurate depiction of the SC morphology is required. More generally, the TR-matching approach could be useful for other SC imaging modalities based on data subtraction such as MT asymmetry (e.g. CEST), arterial spin labeling and fMRI.

The proposed method uses a dedicated TR-matching algorithm to choose relevant data pairs from the individually MT weighted images to form the composite ihMT image. A proper record of the ECG trace, containing appropriate sequence landmarks, is necessary to allow

retrospective extraction of the actual TR values of each image instances. Looping over multiple tolerance values δTR for TR-matching ensures automatic selection of the ihMT composite dataset that maximizes SNR in SC while ensuring minimal ihMTR in CSF ($0\pm\epsilon\%$). The flexibility offered by this automatic selection, rather than using a fixed δTR value for all subjects, ensures individual best SNR conditions independent of the ECG variations and of the actual CSF signal bias. Hence when the TR-matching correction was not necessary to obtain negligible ihMT signal in CSF (e.g. Fig. (6a), data corresponding to 5mm slice and 3500ms nominal TR), the algorithm used the whole dataset to compose the ihMT image. Conversely when strong residual CSF signal was present on the non TR-matched ihMT image, a rather short δTR would be automatically selected, corresponding to a certain amount of data exclusion, yielding the optimal SNR for this experimental scenario as explicitly searched for by the selection algorithm (Fig. 4).

Besides the three ROIs that have to be defined manually (SC, CSF and noise) the only other user-defined parameter is the value of ϵ , i.e. the maximum allowed residual CSF signal. For all acquired data, three different ϵ values were systematically tested: 0.1%, 0.3% and 0.5%. Whereas $\epsilon = 0.1\%$ appeared too restrictive in 33% of the processed datasets (failure in finding a value of δTR fulfilling the condition $|\text{ihMTR}_{\text{CSF}}| < \epsilon$), conditions $\epsilon = 0.3\%$ and $\epsilon = 0.5\%$ yielded satisfying results with respectively only 11% and 4% failures. Of interest, these latter failures all occurred for 50% PE oversampling, hence suggesting that signal blurring may be the cause of such outlier behavior. Indeed, if the residual signal in the CSF area corresponds to actual ihMT signal coming from neighboring CNS tissues, it would not be possible to constrain this signal to zero and the only way to force the algorithm to converge would be to increase ϵ . To summarize, all presented quantitative measurements were obtained using a default ϵ of 0.3%, which was possibly raised to 0.5%, or 0.7%, when necessary and we recommend using similar settings for the general use of this algorithm.

Surprisingly, the ihMTR values measured in SC were significantly lower for the A-P PE direction as compared to the S-I direction (Fig. 7a). The readout-module weighting difference due to 50% phase oversampling (547ms readout duration and 31ms effective TE compared to 365ms readout and 20ms TE without oversampling) could be discarded as a hypothetical explanation for this difference because similar (within error bars) ihMTRs were measured on SC when comparing the A-P direction with and without oversampling. Conversely CSF partial volume effects could be hypothesized as a plausible cause of the underestimation

of ihMTR in the SC for the A-P PE direction. Indeed, even though the CSF ihMT signal is negligible, CSF would increase the reference S_0 signal (especially with a T_2 -weighted HASTE readout), hence leading to underestimation of the ihMT ratio of the contaminated tissue. As already pointed out, partial volume effects could be appreciated on Fig. 4 where the dynamic of ihMTR vs. δ TR measured on SC follows the one from CSF. Moreover these effects were also evidenced in the signal recovery observed in SC (see slope in Fig. 3e) since T_1 -recovery is not expected over this long TR range ($TR \approx 4000$ ms) for CNS tissue at 1.5T (23), and these recovery effects were stronger in the A-P PE direction as compared to S-I (steeper slope in Fig. 7b). Whereas slice profile imperfections could explain some partial volume contribution, it remains unclear why CSF would “blur” onto SC for relatively short readout (300 to 500ms) with A-P PE, especially considering that data have been Hamming-filtered in k-space to prevent non-local signal contamination. However the extension of the cord in the S-I direction likely explains why partial volume with CSF would be more pronounced on data acquired in A-P PE. Finally, measurements performed in the CC, less prone to CSF contamination, yielded similar ihMTR values for the three PE conditions (7a). Compared to SC, reduced and hardly noticeable T_1 -recovery effects were observed in CC for S-I and A-P PE, respectively (see slopes in 3f and 7c), again supporting the CSF signal contamination hypothesis in SC.

A nominal TR value of 3500ms appears to be optimal to maximize both SNR efficiency (for reduced scan time) and robustness, characterized by low inter-subject variability. The global trend of increased SNR efficiency with shorter TR (Fig. 6c) is definitely due to a more efficient use of the timing intervals within the sequence, made possible by proper CSF signal suppression. However, for $TR=2500$ ms the SNR efficiency show strong signs of instability evidenced by larger standard errors for both TR-matched and non TR-matched data. Two combined reasons could explain this phenomenon. On one hand, shorter TR leads to more intense quasi-random value of the CSF ihMTR bias signal for the non TR-matched data, which in turn may affect the SC signal through partial volume effects. On the other hand, the TR-matching algorithm preserves only a finite number of data pairs especially for short TRs, which is also in essence an arbitrary process, and this may translate into strong SNR loss.

Overall it was found that the slice thickness had some impact on the derived metrics measured from C2 to C4 (slightly higher ihMTR values obtained for 5mm slice), likely due to the GM/WM distribution within the cord (24). Although one would like the ideal single-slice sagittal protocol to cover the whole cord extension (about 10-15mm in R-L dimension), hence

prescribing a rather thick slice, it is important to keep in mind that typical HASTE slice profiles are not very sharp. Particular care was deployed to prescribe the slices in this study, using multiple axial T_2^* -weighted images to center the slice positioning in the middle of the cord throughout the R-L direction. However, it is often difficult to reach a perfect alignment of the cord, either because of the subject positioning within the RF-coil or simply because of the natural curvature of the cord. Hence no conclusions should be drawn here about the amount of WM and GM contributing to the measured ihMT signal and we can simply conclude that both slice thicknesses provided reasonable and stable estimation of the SC ihMTR.

Despite different subject populations and slice settings the ihMTR values measured here were found to be in the same range of previous measurements performed on brain (2) at 1.5T for similar energy levels (ihMTR of $8.1 \pm 0.3\%$ in Internal Capsule and $6.7 \pm 0.3\%$ in frontal WM for $E_{TR} \approx 15\text{uT}^2$ vs. ihMTR of $7.8 \pm 0.3\%$ in SC and $7.5 \pm 0.2\%$ in CC for $E_{TR} \approx 17.2\text{uT}^2$ in this study). Here the actual E_{TR} value was kept constant and was chosen to allow scanning within regulatory SAR limit for a nominal TR of 2500ms. Higher energy levels could be considered for a longer TR of 3500ms but a large increase of ihMTR is not anticipated (2).

Finally, although the proposed methodology has been carefully demonstrated here on SC images acquired in the sagittal plane at 1.5T, the same strategy may be readily applied in the axial plane as recently demonstrated at 3T (25), and could be further used to assess the ihMTR distribution within and across the cord. This would for instance be of particular use to further understand the WM-tract microstructure differences (e.g. potential different myelination of sensory and motor tracts) using atlas-based segmentation (26–28) and to assess *in vivo* and non-invasively such features. This would also be very appropriate to go further in the description of the WM impairment in degenerative pathologies such as myelopathy (29), MS, SLA and to evaluate potential therapeutic strategies.

Conclusion

This study aimed at providing a fast and robust protocol for ihMT imaging of the SC, free of CSF pulsatility artifacts. ECG synchronization allowed acquiring stable images with respect to the CSF pulsatile motion, but resulted in variable TRs, which translated into a biased residual ihMT signal from CSF that in turn affected SC delineation and ihMT metrics. Fully relaxed acquisition ($TR > 10\text{s}$) may be used to solve the problem, though at the expense of a poor

SNR efficiency. An alternative method based on retrospective data pairing obtained with a TR-matching semi-automatic algorithm was proposed, allowing improved SNR efficiency and faster acquisition, while offering robust ihMT quantification and exquisite image quality of the SC. This opens great possibility for further *in vivo* characterization of SC physiopathology using MRI.

Acknowledgments

This study was supported by IRME. V.H.P. received support from A*MIDEX (n°ANR-11-IDEX-0001-02) funded by the French Government "Investissements d'Avenir" program. The authors thank Elisabeth Soulier and Véronique Gimenez for help with the volunteer management.

References

1. Varma G, Duhamel G, de Bazelaire C, Alsop DC. Magnetization Transfer from Inhomogeneously Broadened Lines: A Potential Marker for Myelin. *Magn. Reson. Med.* 2015;73:614–622. doi: 10.1002/mrm.25174.
2. Girard OM, Prevost VH, Varma G, Cozzone PJ, Alsop DC, Duhamel G. Magnetization transfer from inhomogeneously broadened lines (ihMT): Experimental optimization of saturation parameters for human brain imaging at 1.5 Tesla. *Magn. Reson. Med.* 2015;73:2111–2121. doi: 10.1002/mrm.25330.
3. Varma G, Girard OM, Prevost VH, Grant AK, Duhamel G, Alsop DC. Interpretation of magnetization transfer from inhomogeneously broadened lines (ihMT) in tissues as a dipolar order effect within motion restricted molecules. *J. Magn. Reson.* 2015;260:67–76. doi: 10.1016/j.jmr.2015.08.024.
4. Baumann N, Pham-Dinh D. Biology of oligodendrocyte and myelin in the mammalian central nervous system. *Physiol. Rev.* 2001;81:871–927.
5. Horch RA, Gore JC, Does MD. Origins of the ultrashort-T2H NMR signals in myelinated nerve: A direct measure of myelin content? *Magn. Reson. Med.* 2011;66:24–31. doi: 10.1002/mrm.22980.
6. Portis AM. Electronic Structure of f Centers: Saturation of the Electron Spin Resonance. *Phys. Rev.* 1953;91:1071–1078. doi: 10.1103/PhysRev.91.1071.
7. Davis JH, Auger M, Hodges RS. High resolution ^1H nuclear magnetic resonance of a transmembrane peptide. *Biophys. J.* 1995;69:1917–1932. doi: 10.1016/S0006-3495(95)80062-7.
8. Chen J-H, Sambol EB, Decarolis P, O'Connor R, Geha RC, Wu YV, Singer S. High-resolution MAS NMR spectroscopy detection of the spin magnetization exchange by cross-relaxation and chemical exchange in intact cell lines and human tissue specimens. *Magn. Reson. Med.* 2006;55:1246–1256. doi: 10.1002/mrm.20889.
9. Vavasour IM, Whittall KP, Li DK, MacKay AL. Different magnetization transfer effects exhibited by the short and long T(2) components in human brain. *Magn. Reson. Med.* 2000;44:860–866.
10. Huster D, Yao X, Hong M. Membrane Protein Topology Probed by ^1H Spin Diffusion from Lipids Using Solid-State NMR Spectroscopy. *J. Am. Chem. Soc.* 2002;124:874–883. doi: 10.1021/ja017001r.
11. Prevost VH, Girard OM, Varma G, Alsop DC, Duhamel G. Magnetization Transfer from Inhomogeneously Broadened Lines (ihMT): Qualitative Evaluation of ihMT Specificity toward Myelinated Structures. In: *Proceedings of the ISMRM. Milan, Italy; 2014.* p. 1498.
12. Varma G, Neema M, Papadopoulou F, Tauhid S, Bakshi R, Alsop DC. Analysis of Inhomogeneous Magnetization Transfer Applied In Patients with Multiple Sclerosis. In: *Proceedings of the ISMRM. Milan, Italy; 2014.* p. 2071.

13. Duhamel G, Le Troter A, Prevost VH, Varma G, Guye M, Ranjeva J-P, Pelletier J, Alsop DC, Girard OM. Magnetization Transfer from Inhomogeneously Broadened Lines (ihMT): Application on Multiple Sclerosis (MS). In: Proceedings of the ISMRM. Toronto, Canada; 2015. p. 4346.
14. Rangwala N, Varma G, Hackney D, Alsop DC. Quantification of myelin in the cervical spinal cord using inhomogeneous magnetization transfer imaging. In: Proceedings of the ISMRM. Salt Lake City, Utah, USA; 2013. p. 350.
15. Girard OM, Callot V, Robert B, Rangwala N, Cozzzone PJ, Alsop DC, Duhamel G. Magnetization Transfer from Inhomogeneously Broadened Lines (ihMT): Improved SC Imaging using ECG Synchronization. In: Proceedings of the ISMRM. Milan, Italy; 2014. p. 3450.
16. Friese S, Hamhaber U, Erb M, Kueker W, Klose U. The influence of pulse and respiration on spinal cerebrospinal fluid pulsation. *Invest. Radiol.* 2004;39:120–130. doi: 10.1097/01.rli.0000112089.66448.bd.
17. Summers P, Staempfli P, Jaermann T, Kwiecinski S, Kollias S. A preliminary study of the effects of trigger timing on diffusion tensor imaging of the human spinal cord. *AJNR Am. J. Neuroradiol.* 2006;27:1952–1961.
18. Kharbanda HS, Alsop DC, Anderson AW, Filardo G, Hackney DB. Effects of cord motion on diffusion imaging of the spinal cord. *Magn. Reson. Med.* 2006;56:334–339. doi: 10.1002/mrm.20959.
19. Guimaraes AR, Melcher JR, Talavage TM, Baker JR, Ledden P, Rosen BR, Kiang NYS, Fullerton BC, Weisskoff RM. Imaging Subcortical Auditory Activity in Humans. *Hum. Brain Mapp.* 1998;6:33–41.
20. Shin J, Ahn S, Hu X. Correction for the T1 effect incorporating flip angle estimated by Kalman filter in cardiac-gated functional MRI. *Magn. Reson. Med.* 2013;70:1626–1633. doi: 10.1002/mrm.24620.
21. Harris FJ. On the use of windows for harmonic analysis with the discrete Fourier transform. *Proc. IEEE* 1978;66:51–83.
22. Penny WD, Friston KJ, Ashburner JT, Kiebel SJ, Nichols TE. *Statistical Parametric Mapping: The Analysis of Functional Brain Images: The Analysis of Functional Brain Images.* Academic Press; 2011.
23. Rooney WD, Johnson G, Li X, Cohen ER, Kim S-G, Ugurbil K, Springer CS. Magnetic field and tissue dependencies of human brain longitudinal $^1\text{H}_2\text{O}$ relaxation in vivo. *Magn. Reson. Med.* 2007;57:308–318. doi: 10.1002/mrm.21122.
24. Taso M, Le Troter A, Sdika M, Ranjeva J-P, Guye M, Bernard M, Callot V. Construction of an in vivo human spinal cord atlas based on high-resolution MR images at cervical and thoracic levels: preliminary results. *Magn Reson Mater Phy MAGMA* 2014;27:257–267. doi: 10.1007/s10334-013-0403-6.
25. Taso M, Girard OM, Duhamel G, Le Troter A, Ribeiro G, Feiweier T, Guye M, Ranjeva J-P, Callot V. Regional and age-related variations of the healthy spinal cord structure assessed

by multimodal MRI (diffusion, inhomogeneous magnetization transfer, ihMT). In: Proceedings of the ISMRM. Toronto, Canada; 2015. p. 681.

26. Lévy S, Benhamou M, Naaman C, Rainville P, Callot V, Cohen-Adad J. White matter atlas of the human spinal cord with estimation of partial volume effect. *NeuroImage* 2015;119:262–271. doi: 10.1016/j.neuroimage.2015.06.040.

27. Fonov VS, Le Troter A, Taso M, et al. Framework for integrated MRI average of the spinal cord white and gray matter: The MNI-Poly-AMU template. *NeuroImage* 2014;102 Pt 2:817–827. doi: 10.1016/j.neuroimage.2014.08.057.

28. Taso M, Le Troter A, Sdika M, Cohen-Adad J, Arnoux P-J, Guye M, Ranjeva J-P, Callot V. A reliable spatially normalized template of the human spinal cord - Applications to automated white matter/gray matter segmentation and tensor-based morphometry (TBM) mapping of gray matter alterations occurring with age. *NeuroImage* 2015;117:20–28. doi: 10.1016/j.neuroimage.2015.05.034.

29. Taso M, Girard OM, Duhamel G, Feiweier T, Arnoux P-J, Guye M, Ranjeva J-P, Chaumoitre K, Roche P-H, Callot V. Cervical myelopathy patient follow-up after decompressive surgery using diffusion tensor imaging (DTI) and inhomogeneous magnetization transfer (ihMT): preliminary application and results. In: Proceedings of the ISMRM. Toronto, Canada; 2015. p. 4426.

Figure captions:

Figure 1: Effect of k-space windowing demonstrated on T_2 weighted HASTE SC data. Low spatial resolution of SC images leads to significant Gibb's ringing in the SC area: 2-times zero-filled images (i.e. boxcar window (a)) demonstrate signal oscillations in the SC whereas Hamming windowed data (b) improves MR signal fidelity of SC by removing CSF secondary lobe contamination, though at the expenses of signal blurring. Theoretical expectations of the ideal point spread function (at infinite T_2) for Cartesian sampling using both windows are shown in (c).

Figure 2: Effect of ECG synchronization on SC data. (a) Reference ECG triggered anatomical scan (T2w FSE) and corresponding MTR (b) and ihMTR (c) map obtained using optimized protocol (ECG synchronization and retrospective data pairing for ihMT). Examples of non-triggered acquisitions acquired on two different volunteers are displayed in (d) - (g). Whereas MTR data do not evidence strong signs of motion artifacts in the cord area (d) and (e), the ihMTR data reconstructed from the same datasets show particularly strong CSF pulsatile artifacts ((f) and (g), green arrows), consistent with increased motion sensitivity of an image-subtraction based technique. ECG synchronization combined with the retrospective bias correction algorithm recovers exquisite SC image quality (c).

Figure 3: Scatter plots of all individual MT weighted signals (single- and dual-frequency saturation) measured during one full ihMT acquisition in CSF, SC and CC. The signals are plotted vs. the NEX index for the non-triggered acquisition in (a), (b) and (c) and vs. the actual TRs for the triggered acquisition in (d), (e) and (f). For each structure, the MR signal was normalized by the average MR signal measured over all instances of the four kinds of MT weighted images. Presented data were acquired with an 8mm slice and phase encoding in the S-I direction. Steep T_1 recovery is evidenced for CSF over this TR range in d), and modest recovery occurs in the SC and CC data in (e). Linear regression plots and corresponding slopes are indicated to help appreciate the T_1 recovery effects. For CSF, single- and dual-frequency data clouds are overlapping, consistent with no ihMT effect. For SC, non-triggered acquisition (b) yields partially overlapping data clouds, consistent with pulsatile artifact and partial volume from CSF, whereas triggered acquisition shows clear separation of single- and dual-frequency data clouds (e). For CC, good separation of single- and dual-frequency data clouds is observed in both cases, evidencing strong ihMT effect, and illustrating less motion sensitivity. Examples of ROIs used for SCF, SC and CC measurements are shown on the S_0 image at the center.

Figure 4: Principle of the automatic TR-matching algorithm illustrated on two particularly demonstrative datasets. Because of the random nature of ECG rate fluctuations the residual CSF ihMT signal that is observed when no TR-matching filtering is used may be arbitrarily positive, (a) and (d), or negative, (b) and (f). For long δTR (e.g. $>800ms$ here) the whole dataset is considered to form the composite ihMTR images, hence leading to the biased images shown on the bottom-right side of each panel, (d) and (f). As δTR is shortened, selective TR-matched ($\pm \delta TR$) pairs of MT images are automatically selected by the algorithm and the corresponding ihMTR measured in CSF is progressively constrained to $0 \pm \epsilon$ %. The best TR-matched datasets, automatically chosen by the algorithm (indicated by the blue vertical lines), result from a compromise between the lowest ihMTR in CSF and the highest SNR in the SC, leading to the unbiased ihMTR images shown on the bottom-left side of each panel, (c) and (e). Note that case 1 was acquired with PE set to S-I and a nominal TR of 2500ms, whereas PE was set to A-P and the nominal TR was 3500ms for case 2.

Figure 5: Demonstration of the efficiency of the TR-matching algorithm for three different nominal TRs: 2500ms, 3500ms and 10000ms (i.e. full-relaxed CSF dataset). CSF signal recovery over the actual TR ranges are strong (a), moderate (b) and very low (c), hence yielding to strong, moderate and negligible CSF signal bias on the corresponding unfiltered ihMTR images (no TR-matching, (d)-(f)), respectively. Conversely, in all cases the best TR-matched ihMTR images ((g)-(i)) show negligible CSF signal (as in the unfiltered full relaxed dataset shown in (f)) hence providing high-fidelity ihMTR maps over the cervical SC. $\varepsilon = 0.3\%$ was used here. The fully relaxed acquisition yielded $\text{ihMTR}_{\text{CSF}} \approx 0.45\%$ with no TR-matching in (f).

Figure 6: Quantitative evaluation of the TR-matching strategy in terms of ihMTR and SNR efficiency. While the CSF signal bias was particularly strong (a) for short nominal TRs (e.g. 2500ms) and led to instability of the SC ihMTR (relatively large error bars), the TR-matching strategy satisfactorily constrained the CSF to $0 \pm \varepsilon$ % and reduced SC data inter-subject variability for short TRs (b). Note that both SC and CSF ihMTR are particularly stable over the whole TR range in (b). The corresponding ihMT SNR efficiency (c) is a quantitative index of the SNR improvement and consequently shorter acquisition time made possible by the use of short TRs and allows appreciating SNR losses due to data-pair exclusion (see text for more details). All data in (a)-(c) were acquired with S-I PE direction. A target ε of 0.3% was used for all data (see text for more details).

Figure 7: Comparison of the ihMTR measured in SC and CC for both S-I and A-P PE directions (a) suggest that S-I direction should be preferred to avoid residual bias leading to strong underestimation of SC metrics. Conversely the CC ihMTR are in very good agreement for both PE directions. Panels (b) and (c) display scatter plots similar to Fig. 3 (e) and (f) except that the phase encoding was set to A-P with 50% phase oversampling. Linear regression plots and corresponding slopes are indicated to help appreciate the T_1 recovery effect and compare with S-I data from Fig.3. A much steeper T_1 recovery is observed for the SC ROI in (b) as compared the plot from Fig. 3 (e) suggesting stronger partial volume effects from CSF. All data were acquired using TR=3500ms, a 5mm slice and a target ε of 0.3%.

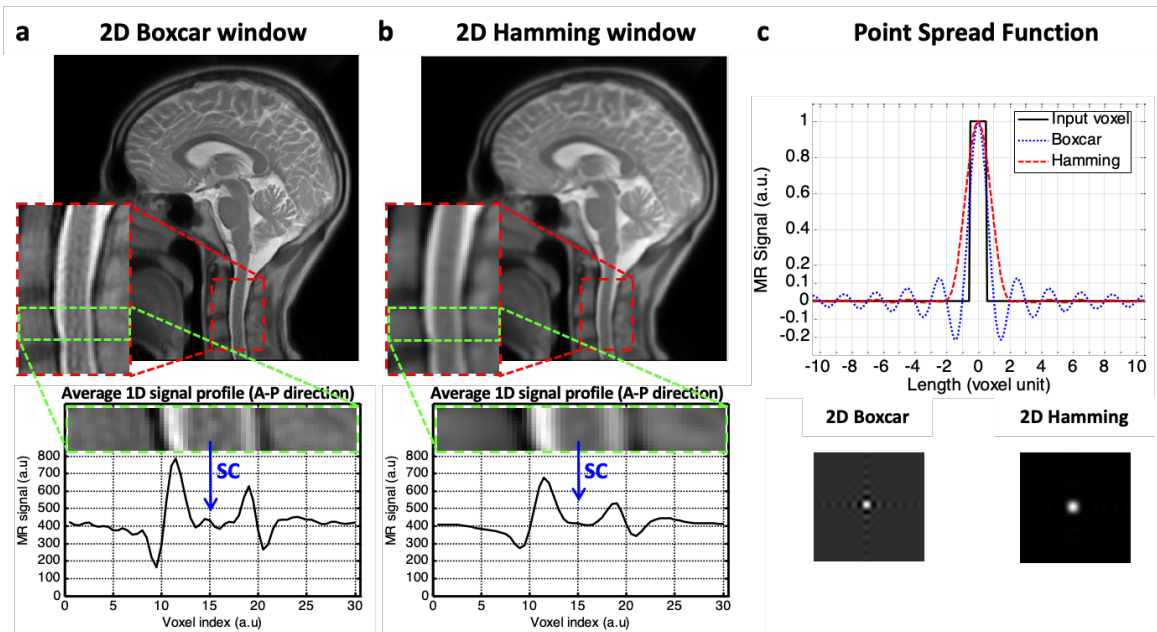


Fig. 1: Effect of k-space windowing demonstrated on T_2 weighted HASTE SC data. Low spatial resolution of SC images leads to significant Gibbs's ringing in the SC area: 2-times zero-filled images (i.e. boxcar window (a)) demonstrate signal oscillations in the SC whereas Hamming windowed data (b) improves MR signal fidelity of SC by removing CSF secondary lobe contamination, though at the expenses of signal blurring. Theoretical expectations of the ideal point spread function (at infinite T_2) for Cartesian sampling using both windows are shown in (c).

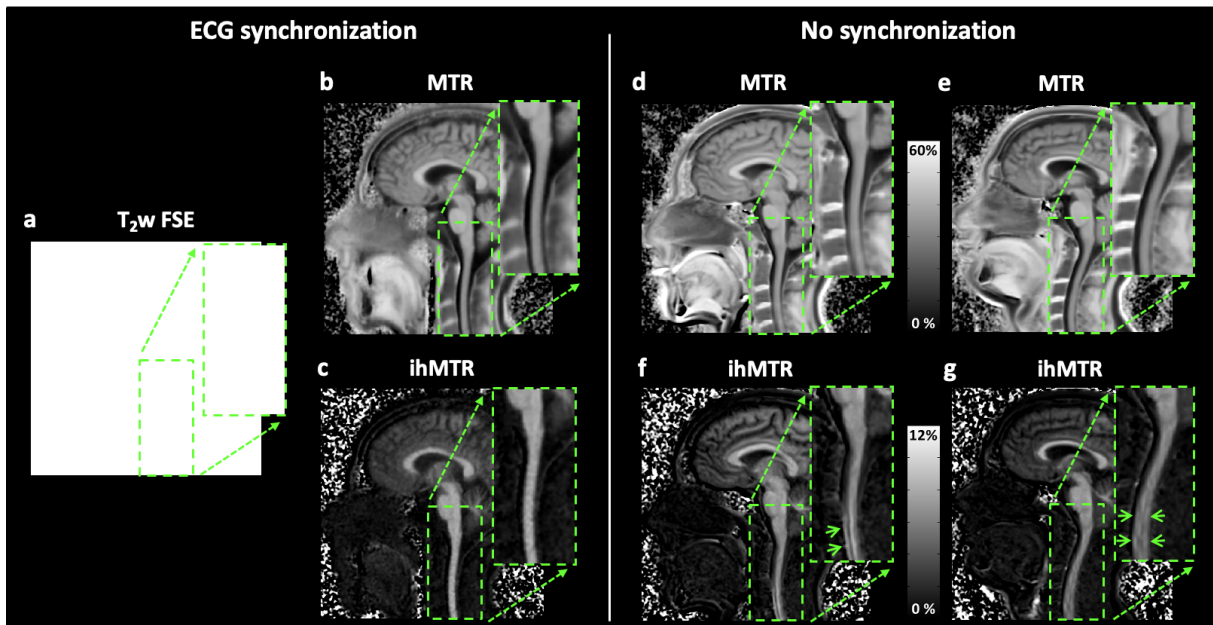


Fig. 2: Effect of ECG synchronization on SC data. (a) Reference ECG triggered anatomical scan (T_2 w FSE) and corresponding MTR (b) and ihMTR (c) map obtained using optimized protocol (ECG synchronization and retrospective data pairing for ihMT). Examples of non-triggered acquisitions acquired on two different volunteers are displayed in (d) - (g). Whereas MTR data do not evidence strong signs of motion artifacts in the cord area (d) and (e), the ihMTR data reconstructed from the same datasets show particularly strong CSF pulsatile artifacts ((f) and (g), green arrows), consistent with increased motion sensitivity of an image-subtraction based technique. ECG synchronization combined with the retrospective bias correction algorithm recovers exquisite SC image quality (c).

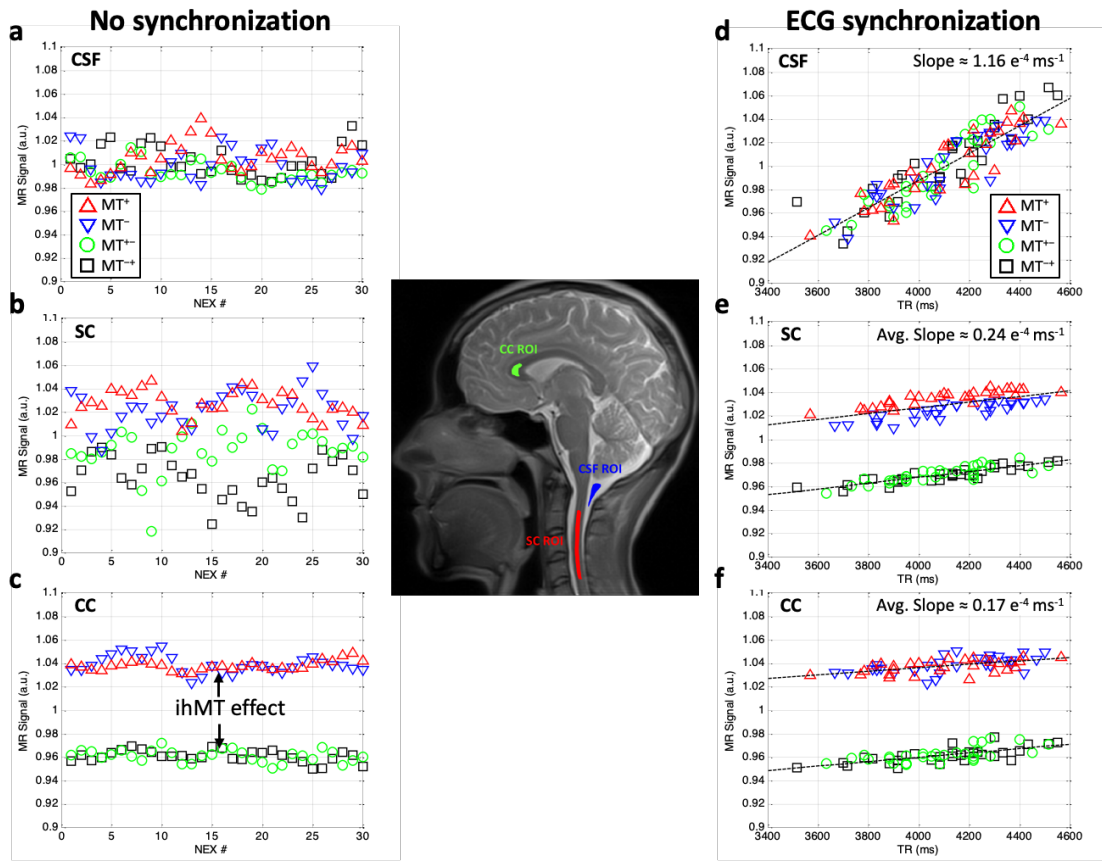


Fig. 3: Scatter plots of all individual MT weighted signals (single- and dual-frequency saturation) measured during one full ihMT acquisition in CSF, SC and CC. The signals are plotted vs. the NEX index for the non-triggered acquisition in (a), (b) and (c) and vs. the actual TRs for the triggered acquisition in (d), (e) and (f). For each structure, the MR signal was normalized by the average MR signal measured over all instances of the four kinds of MT weighted images. Presented data were acquired with an 8mm slice and phase encoding in the S-I direction. Steep T_1 recovery is evidenced for CSF over this TR range in d), and modest recovery occurs in the SC and CC data in (e). Linear regression plots and corresponding slopes are indicated to help appreciate the T_1 recovery effects. For CSF, single- and dual-frequency data clouds are overlapping, consistent with no ihMT effect. For SC, non-triggered acquisition (b) yields partially overlapping data clouds, consistent with pulsatile artifact and partial volume from CSF, whereas triggered acquisition shows clear separation of single- and dual-frequency data clouds (e). For CC, good separation of single- and dual-frequency data clouds is observed in both cases, evidencing strong ihMT effect, and illustrating less motion sensitivity. Examples of ROIs used for SCF, SC and CC measurements are shown on the S_0 image at the center.

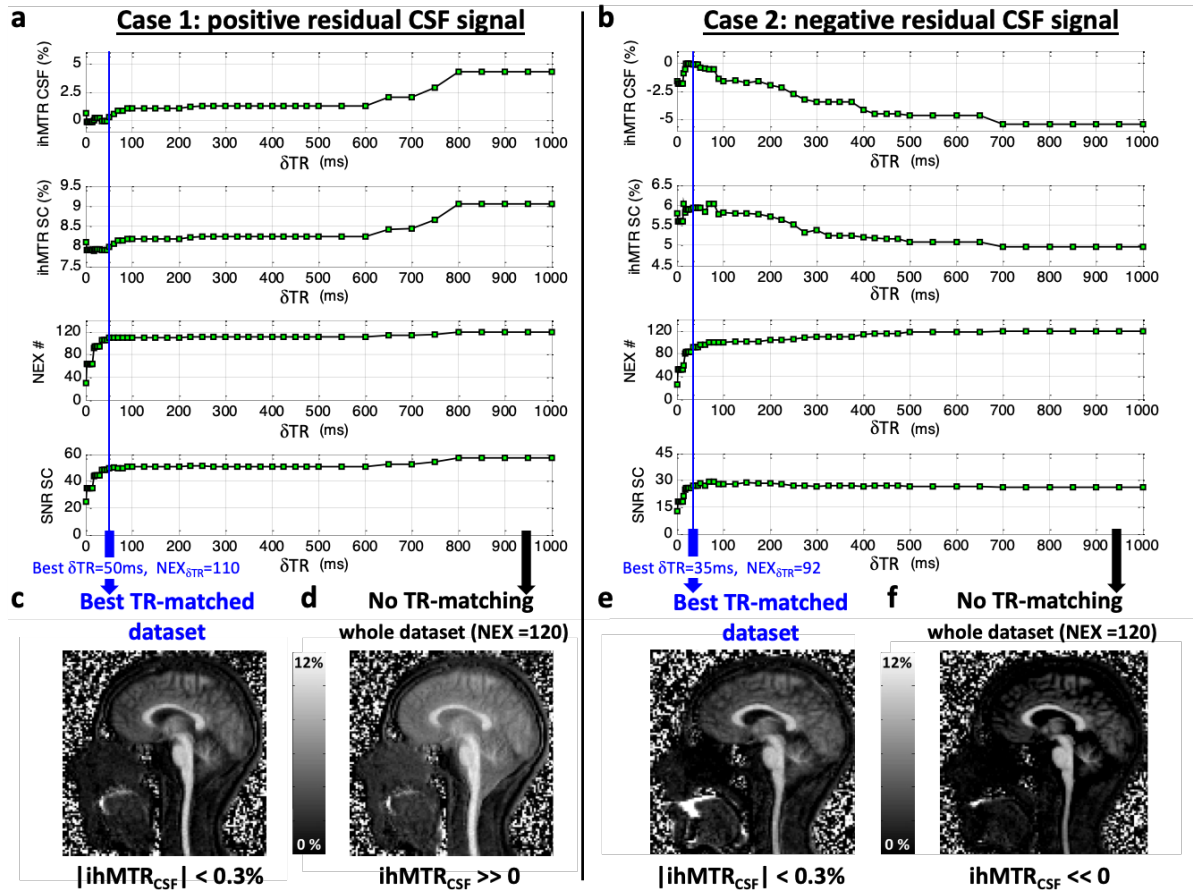


Fig. 4: Principle of the automatic TR-matching algorithm illustrated on two particularly demonstrative datasets. Because of the random nature of ECG rate fluctuations the residual CSF ihMT signal that is observed when no TR-matching filtering is used may be arbitrarily positive, (a) and (d), or negative, (b) and (f). For long δTR (e.g. $>800\text{ms}$ here) the whole dataset is considered to form the composite ihMTR images, hence leading to the biased images shown on the bottom-right side of each panel, (d) and (f). As δTR is shortened, selective TR-matched ($\pm \delta TR$) pairs of MT images are automatically selected by the algorithm and the corresponding ihMTR measured in CSF is progressively constrained to $0 \pm \epsilon$ %. The best TR-matched datasets, automatically chosen by the algorithm (indicated by the blue vertical lines), result from a compromise between the lowest ihMTR in CSF and the highest SNR in the SC, leading to the unbiased ihMTR images shown on the bottom-left side of each panel, (c) and (e). Note that case 1 was acquired with PE set to S-I and a nominal TR of 2500ms, whereas PE was set to A-P and the nominal TR was 3500ms for case 2.

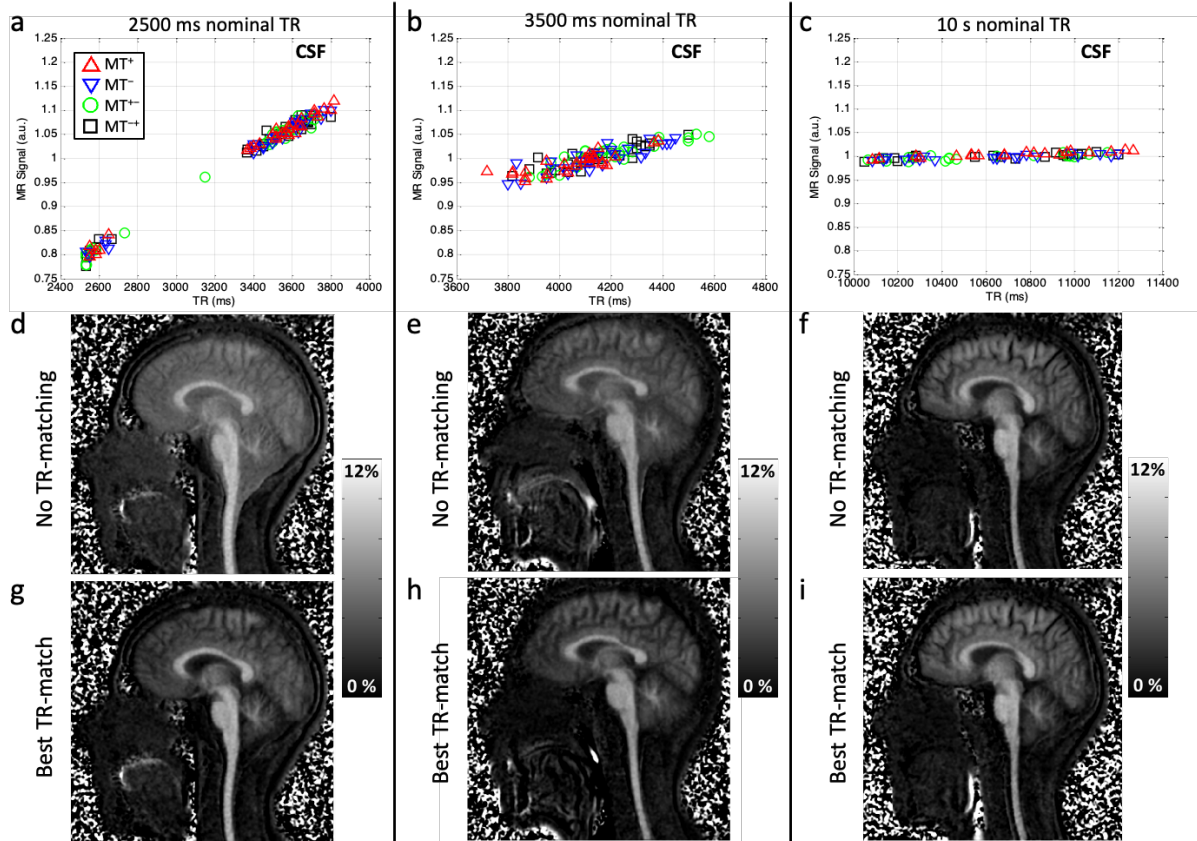


Fig. 5: Demonstration of the efficiency of the TR-matching algorithm for three different nominal TRs: 2500ms, 3500ms and 10000ms (i.e. full-relaxed CSF dataset). CSF signal recovery over the actual TR ranges are strong (a), moderate (b) and very low (c), hence yielding to strong, moderate and negligible CSF signal bias on the corresponding unfiltered ihMTR images (no TR-matching, (d)-(f)), respectively. Conversely, in all cases the best TR-matched ihMTR images ((g)-(i)) show negligible CSF signal (as in the unfiltered full relaxed dataset shown in (f)) hence providing high-fidelity ihMTR maps over the cervical SC. $\epsilon = 0.3\%$ was used here. The fully relaxed acquisition yielded $\text{ihMTR}_{\text{CSF}} \approx 0.45\%$ with no TR-matching in (f).

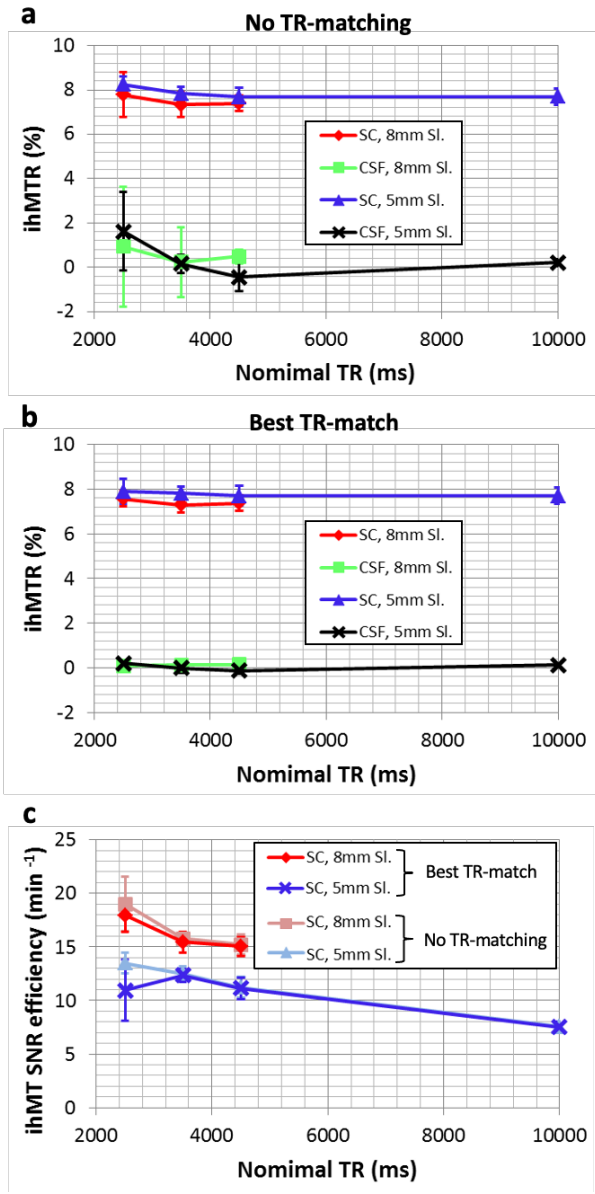


Fig. 6: Quantitative evaluation of the TR-matching strategy in terms of ihMTR and SNR efficiency. While the CSF signal bias was particularly strong (a) for short nominal TRs (e.g. 2500ms) and led to instability of the SC ihMTR (relatively large error bars), the TR-matching strategy satisfactorily constrained the CSF to $0 \pm \epsilon$ % and reduced SC data inter-subject variability for short TRs (b). Note that both SC and CSF ihMTR are particularly stable over the whole TR range in (b). The corresponding ihMT SNR efficiency (c) is a quantitative index of the SNR improvement and consequently shorter acquisition time made possible by the use of short TRs and allows appreciating SNR losses due to data-pair exclusion (see text for more details). All data in (a)-(c) were acquired with S-I PE direction. A target ϵ of 0.3% was used for all data (see text for more details).

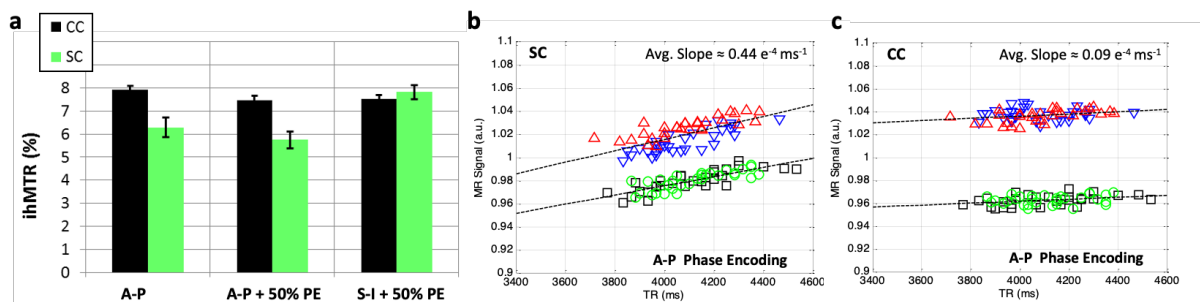


Fig. 7: Comparison of the ihMTR measured in SC and CC for both S-I and A-P PE directions (a) suggest that S-I direction should be preferred to avoid residual bias leading to strong underestimation of SC metrics. Conversely the CC ihMTR are in very good agreement for both PE directions. Panels (b) and (c) display scatter plots similar to Fig. 3 (e) and (f) except that the phase encoding was set to A-P with 50% phase oversampling. Linear regression plots and corresponding slopes are indicated to help appreciate the T_1 recovery effect and compare with S-I data from Fig.3. A much steeper T_1 recovery is observed for the SC ROI in (b) as compared the plot from Fig. 3 (e) suggesting stronger partial volume effects from CSF. All data were acquired using TR=3500ms, a 5mm slice and a target ϵ of 0.3%.